

# Flow-matching – efficient coarse-graining molecular dynamics without forces

Jonas Köhler<sup>a,1</sup>, Yaoyi Chen<sup>a,1</sup>, Andreas Krämer<sup>a,1,2</sup>, Cecilia Clementi<sup>b,c,d,e,2</sup>, and Frank Noé<sup>a,b,e,f,2</sup>

<sup>a</sup>Department of Mathematics and Computer Science, Freie Universität Berlin, Arnimallee 12, 14195 Berlin, Germany; <sup>b</sup>Department of Physics, Freie Universität Berlin, Arnimallee 12, 14195 Berlin, Germany; <sup>c</sup>Center for Theoretical Biological Physics, Rice University, Houston, TX 77005, USA; <sup>d</sup>Department of Physics, Rice University, Houston, TX 77005, USA; <sup>e</sup>Department of Chemistry, Rice University, Houston, TX 77005, USA; <sup>f</sup>Microsoft Research Cambridge, United Kingdom

**Coarse-grained (CG) molecular simulations have become a standard tool to study molecular processes on time- and length-scales inaccessible to all-atom simulations. Parameterizing CG force fields to match all-atom simulations has mainly relied on force-matching or relative entropy minimization, which require many samples from costly simulations with all-atom or CG resolutions, respectively. Here we present *flow-matching*, a new training method for CG force fields that combines the advantages of both methods by leveraging normalizing flows, a generative deep learning method. Flow-matching first trains a normalizing flow to represent the CG probability density, which is equivalent to minimizing the relative entropy without requiring iterative CG simulations. Subsequently, the flow generates samples and forces according to the learned distribution in order to train the desired CG energy model via force matching. Even without requiring forces from the all-atom simulations, flow-matching outperforms classical force-matching by an order of magnitude in terms of data efficiency, and produces CG models that can capture the folding and unfolding transitions of small proteins.**

coarse-graining | force field | machine learning | generative model

Molecular dynamics (MD) simulations have become a major computational tool to study biophysical processes on molecular scales. Presently, MD simulations at all-atom resolution can reach multiple microseconds for small to medium-sized protein systems on retail hardware. By using special-purpose Anton supercomputers (1, 2) or combining distributed computing with Markov State Modeling (3, 4) or enhanced sampling approaches, it is possible to probe millisecond-timescales and sometimes beyond (5, 6).

Despite this progress, many biomolecular processes of interest exceed these time and length scales by orders of magnitude. Also high-throughput simulations that would be needed, e.g., to screen protein sequences for high-affinity protein-protein interactions, cannot be efficiently done with all-atom MD.

A common approach to go to larger time- and length-scales or high-throughput simulations, is coarse-grained (CG) molecular dynamics (7–22). In “bottom-up” coarse-graining, one defines a mapping from the all-atom representation to the CG model (e.g. by grouping sets of atoms to coarse-grained beads). The choice of mapping determines the resolution and has to suit the system as well as the scientific question, which is by itself a challenge (13, 16, 23, 24). Given that the CG mapping is chosen, a frequently used CG principle is known as thermodynamic consistency in the coarse-graining literature and as density matching in machine learning: the CG model should generate the same equilibrium distribution, as one would obtain from a fully converged all-atom simulation after applying the coarse-graining map to all simulation frames (13). In principle, the requirement of thermodynamic consistency uniquely defines the effective energy function for the CG model,

which is also known as the *potential of mean force* (PMF). Provided that the quantities of interest can still be computed from the coarse-grained representation of the molecule, the PMF is the “exact” effective coarse-grained energy function that can predict the same thermodynamic quantities as the all-atom ground truth model. However, the PMF by definition involves high dimensional integrals that cannot be estimated for nontrivial systems in practice. A pivotal challenge is to find a good approximation for the PMF with tractable functional forms to serve as the CG potential (13).

Among the techniques for such bottom-up modeling (13, 15, 25–28), two methods have been explicitly developed to approach thermodynamic consistency: variational force-matching (also known as multi-scale coarse graining) (26, 27) and relative entropy minimization (28). Force-matching (Fig. 1a) is straightforward to implement but requires the forces on the CG particles from all-atom sampling. Because these instantaneous forces depend on all degrees of freedom, they provide a very noisy signal that makes training the CG force field data inefficient. This approach has been connected with the blooming field of machine-learned potentials and led to several successes (20–22). Relative entropy minimization (Fig. 1b), as well as the related method of Iterative Boltzmann Inversion (25), do not require forces to be recorded and are more data-efficient, but require the CG model to be re-simulated during the iterative training procedure, which can make training extremely costly and even lead to failure in convergence.

## Significance Statement

All-atom molecular dynamics simulations are an important tool to study biological processes, but are limited to relatively small systems and short time scales. In this work, we present “flow-matching”, an efficient method for building coarse-grained models that can reach much larger scales but still agree well with atomistic simulations. Flow-matching combines classical coarse-graining principles with generative machine learning. The generative models take the crucial role of sampling coarse-grained configurations and equipping them with force information. We show that this workflow outperforms established methods for building coarse-grained protein models and that it can recover the folding and unfolding mechanisms of small proteins with high accuracy.

Author contributions: J.K., Y.C., A.K., C.C., and F.N. designed research; J.K., Y.C., and A.K. performed research; J.K., Y.C., A.K., and F.N. analyzed data; J.K., Y.C., A.K., C.C., and F.N. wrote the paper.

The authors declare no competing interests.

<sup>1</sup>J.K., Y.C. and A.K. contributed equally to this work.

<sup>2</sup>E-mail: {andreas.kraemer, cecilia.clementi, frank.noel}@fu-berlin.de

This manuscript presents a third alternative—the *flow-matching* method, which proved to be more efficient. Our approach combines aspects of force-matching and relative entropy minimization with deep generative modeling. The centerpiece of this novel method is a *normalizing flow* (29–31), a generative neural network that can approximate arbitrary probability distributions by transforming them into simple, easy-to-sample prior distributions. Once trained, normalizing flows can generate uncorrelated samples and compute normalized probability densities, energies, and forces, which makes them an exciting emerging tool for physical applications (32–38). For example, Boltzmann generators (32) use flows that are trained on MD data and energies as one-shot importance samplers for molecular equilibrium distributions.

Flow-matching applies normalizing flows to the coarse-graining problem. Like force-matching and relative entropy minimization, it starts from CG samples in equilibrium, which are usually created by mapping snapshots from an all-atom simulation to the CG space. In order to find a thermodynamically consistent CG potential, the method proceeds in two steps (Fig. 1c). First, a normalizing flow is trained by density matching, such that it learns to sample directly from the target ensemble. Second, the CG equilibrium distribution that the flow has learned is taught to a CG force field by force-matching to coordinate/force pairs generated by the flow.

While this stepwise approach leans on the same underlying principles as previous coarse-graining methods, it avoids their key limitations. In contrast to force-matching (Fig. 1a,c), it does not rely on atomistic reference forces, which are usually not stored in MD simulations. Furthermore, the flow can generate an indefinite number of “synthetic” configurations and forces, which do not carry noise from the atomistic environment. In contrast to relative entropy minimization (28) and iterative Boltzmann inversion (25), flow-matching does not require continuously re-simulating the CG model during training, as the flow can generate independent samples that represent the thermodynamic equilibrium (Fig. 1b,c).

Using the flow only as an intermediate offers complete freedom in choosing the functional form of the final CG force field. In particular, the candidate potential can incorporate the desired physical symmetries and asymptotics (20, 21) as well as share parameters across chemical space (22). Conversely, directly using a normalizing flow as the CG force field would not be a good idea, because transferable properties cannot be easily incorporated into invertible (29, 31) or at least statistically reversible (39) neural networks, which are required by the flows. To this end, flow-matching combines the advantages of normalizing flows and energy-based models in a novel and efficient way.

As a proof of concept, we apply the method to the coarse-graining of small protein systems. We show that accurate CG models can be fit to equilibrium trajectories without using atomistic forces or intermediate simulations. Even when forces are available, we find that flow-matching is much more data-efficient than force-matching and yields surprisingly accurate force fields on small data sets.

## Coarse-graining with Flow-matching

**Coarse-graining with thermodynamic consistency.** We consider a molecular system with atomic coordinates  $\mathbf{R} \in \mathbb{R}^{3N}$  in thermodynamic equilibrium following an equilibrium distribu-

tion

$$\mu(\mathbf{R}) \propto \exp(-u(\mathbf{R})) \quad [1]$$

where  $u$  is the reduced potential energy of the system, whose exact form depends on the choice of the ensemble, e.g.  $u(\mathbf{R}) = U(\mathbf{R})/kT$  for the canonical ensemble with potential energy  $U(\mathbf{R})$ , temperature  $T$  and Boltzmann constant  $k$ .

Coarse-graining considers a mapping  $\Xi: \mathbb{R}^{3N} \rightarrow \mathbb{R}^{3n}$  that projects fine-grained states  $\mathbf{R}$  onto a lower-dimensional representation  $\mathbf{r}$ . In the present work, we only consider linear and orthogonal maps,  $\mathbf{r} = \Xi\mathbf{R}$ . For non-orthogonal or even nonlinear maps, the subsequent mathematical treatment must be generalized (40). As an example, the conformational dynamics of a protein with  $N$  atoms can be projected onto a chosen set of beads by only considering the  $C_\alpha$ -atoms in the backbone. Coarse graining with thermodynamic consistency aims at parameterizing a CG model which yields the same density over the coarse-grained coordinates as the marginal distribution from the original system, i.e.,

$$\nu(\mathbf{r}) = \int d\mathbf{R} \mu(\mathbf{R}) \cdot \delta_{[\Xi\mathbf{R}=\mathbf{r}]}(\mathbf{R}). \quad [2]$$

The CG model is often defined by a CG potential  $V(\cdot; \theta_{\text{pot}})$  with parameters:  $\nu(\cdot; \theta_{\text{pot}}) \propto \exp(-V(\cdot; \theta_{\text{pot}}))$ . Two conventional parameterization approaches will be introduced below.

**Variational force matching.** One option is to optimize a candidate potential  $V(\cdot; \theta_{\text{pot}})$  with the force information from the ground-truth potential  $u$  (Fig 1a). Given a set of fine-grained samples (e.g., MD trajectory)  $\mathcal{D} = (\mathbf{R}_1, \dots, \mathbf{R}_T)$  with corresponding forces  $\mathbf{f}(\mathbf{R}) = -\nabla u(\mathbf{R})$ , it is shown that the thermodynamically consistent CG potential (Eq. 2) can be approximated by the potential minimizing the *variational force-matching loss* (27)

$$\mathcal{L}(\theta_{\text{pot}}) = \mathbb{E}_{\mathbf{R}, \mathbf{f} \sim \mathcal{D}} [\|\Xi_f \mathbf{f} + \nabla_{\Xi\mathbf{R}} V(\Xi\mathbf{R}; \theta_{\text{pot}})\|_2^2], \quad [3]$$

in which  $\Xi_f$  is a force mapping operator dependent on map  $\Xi$ . When infinite samples  $\mathcal{D}$  and all functional forms for  $V$  are available, the minimization of the loss (Eq. (3)) yields exactly the thermodynamically consistent potential defined by Eq. (2). Even with finite samples and restrictions on the  $V(\cdot; \theta_{\text{pot}})$ , the result from the loss minimization still provides a variational approximation in practice. Because of their enhanced expressivity, neural networks with physical inductive biases have been shown to be a useful model class for the parameterization of  $V(\cdot; \theta_{\text{pot}})$  (20, 22).

**Density estimation / relative entropy method.** Force matching requires the mapped CG forces to be saved during fine-grained sampling, which is not common practice. Alternatively, one can directly learn a CG model via density estimation on the observed conformational space. Density estimation aims at minimizing the following objective

$$\mathcal{L}(\theta_{\text{pot}}) = \mathbb{E}_{\mathbf{R} \sim \mathcal{D}} [-\log \nu(\Xi\mathbf{R}; \theta_{\text{pot}})]. \quad [4]$$

The minimizer can be interpreted as the maximum-likelihood solution of an energy-based model trained on the projected samples  $\Xi\mathcal{D} = (\Xi\mathbf{R}_1, \dots, \Xi\mathbf{R}_T)$ . This approach can be related to the relative entropy method in molecular simulation (28) and is used for training an energy-based model in the field of

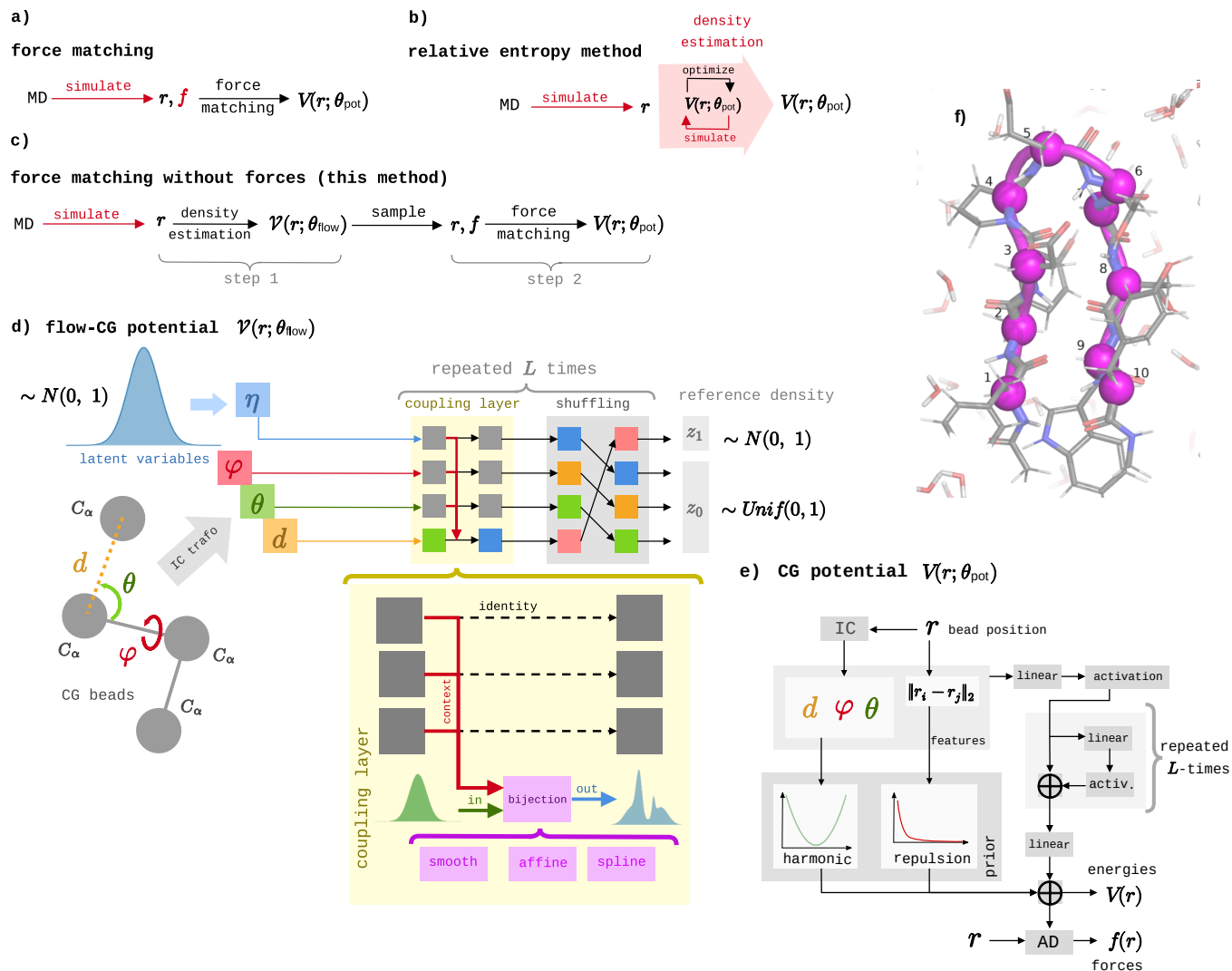


**Fig. 1.** Overview of the flow-matching method. **a)** Classical force-matching: the parameters  $\theta_{\text{pot}}$  of a coarse-grained potential  $V(\cdot; \theta_{\text{pot}})$  are optimized to minimize the mean-squared error of model forces with respect to projected atomistic forces  $f$  on the training configurations  $r$ . **b)** Relative entropy methods: simulations are performed with the coarse-grained potential to produce samples and enable evaluating (and minimizing) the relative entropy. **c)** Present method: the parameters  $\theta_{\text{flow}}$  of a normalizing flow are first optimized to match the CG density from the ground-truth samples  $r$ . This defines the flow-based potential  $V(\cdot; \theta_{\text{flow}})$ . The samples and forces from the flow are used to train a coarse-grained potential  $V(\cdot; \theta_{\text{pot}})$  via force-matching. Slow/inaccurate sampling steps are highlighted in red. **d)** The normalizing flow architecture used in this work to model  $V(\cdot; \theta_{\text{flow}})$ . After transforming the CG beads into an internal coordinate (IC) representation made from bonds ( $d$ ), angles ( $\theta$ ), and dihedral torsions ( $\varphi$ ) a trainable stack of coupling layers transform them into uniform noise. **e)** The modified *CG-Net* architecture used in this work to model  $V(\cdot; \theta_{\text{pot}})$ . “AD” stands for automatic differentiation. **f)** Chignolin in explicit solvent. The magenta spheres show the CG beads of the  $C_\alpha$  model.

machine learning (41). Unfortunately, computing the gradients of Eq. (4) with respect to parameters generates a sampling problem. Computing the gradient contribution of the normalizing constant involves sampling from the model density  $\nu$ , which means that the CG model needs to be periodically re-sampled during training (Fig 1b).

**Flow-based density estimation.** We can avoid the sampling problem of Eq. (4) by using the density  $\nu(\cdot; \theta_{\text{flow}})$  corresponding to a model that can be efficiently sampled, such as normalizing flows (29–31). Flows are invertible neural networks  $\Phi(\cdot; \theta_{\text{flow}}): \mathbb{R}^n \rightarrow \mathbb{R}^n$  that transform an easy-to-sample reference distribution  $q(\mathbf{z})$ , e.g., a Gaussian or uniform density, into our target density. If we sample  $\mathbf{z} \sim q(\mathbf{z})$  and transform it into  $\mathbf{r} = \Phi(\mathbf{z}; \theta_{\text{flow}})$  the resulting density is given by

$$p(\mathbf{r}; \theta_{\text{flow}}) = q(\Phi^{-1}(\mathbf{r}; \theta_{\text{flow}})) \cdot |J_{\Phi^{-1}}(\mathbf{r}; \theta_{\text{flow}})|. \quad [5]$$

Inserting Eq. (5) into Eq. (4) we get an efficient training objective. After training, the energy of the normalizing flow

$$\mathcal{V}(\mathbf{r}; \theta_{\text{flow}}) = -\log p(\mathbf{r}; \theta_{\text{flow}}) \quad [6]$$

approximates the CG PMF.

**Variational density estimation.** Direct density estimation with flow models suffers from the fact that the flow architecture is constrained in order to represent an invertible function, which compromises their representative power and training dynamics. As a solution, we consider relaxing the bijectivity constraint by introducing  $k$  additional variables and sampling a joint state  $\mathbf{z} = (\mathbf{z}_0, \mathbf{z}_1) \in \mathbb{R}^{n+k}$  from a joint (Gaussian/uniform) reference density  $q(\mathbf{z}_0, \mathbf{z}_1)$ . Now we define  $\Phi$  as an invertible coordinate transformation (e.g., a flow model) over those joint  $n+k$  degrees of freedom. Similarly as before, we get the output density  $p(\mathbf{r}, \boldsymbol{\eta}; \theta_{\text{flow}})$  of a transformed pair  $(\mathbf{r}, \boldsymbol{\eta}) = \Phi(\mathbf{z}_0, \mathbf{z}_1; \theta_{\text{flow}})$ . The marginal density over  $\mathbf{r}$  of this augmented model cannot be computed efficiently. However, we can still optimize a variational bound of the likelihood: we first define a joint density  $\nu(\mathbf{r}, \boldsymbol{\eta}) = \nu(\mathbf{r}) \cdot \tilde{\nu}(\boldsymbol{\eta}|\mathbf{r})$  by introducing a Gaussian conditional density  $\tilde{\nu}(\boldsymbol{\eta}|\mathbf{r})$  and then minimize

$$\begin{aligned} \mathcal{L}(\theta_{\text{flow}}) &= \mathbb{E}_{\mathbf{R} \sim \mathcal{D}, \boldsymbol{\eta} \sim \tilde{\nu}(\boldsymbol{\eta}|\mathbf{r})} [-\log p(\boldsymbol{\Xi}\mathbf{R}, \boldsymbol{\eta}; \theta_{\text{flow}})] \\ &\geq \mathbb{E}_{\mathbf{R} \sim \mathcal{D}} [-\log p(\boldsymbol{\Xi}\mathbf{R}; \theta_{\text{flow}})]. \end{aligned} \quad [7]$$

While such *augmented normalizing flows* (42, 43) allow to break topological barriers and satisfy general density approximation guarantees (39, 44), they come at the cost that the density  $p(\mathbf{r}; \theta_{\text{flow}})$ , and thus  $\mathcal{V}(\mathbf{r}, \theta_{\text{flow}})$  as well as the corresponding forces, can no longer be computed. However, we can still compute a joint energy model over CG coordinates and latent variables

$$\mathcal{V}(\mathbf{r}, \boldsymbol{\eta}; \theta_{\text{flow}}) = -\log p(\mathbf{r}, \boldsymbol{\eta}; \theta_{\text{flow}}), \quad [8]$$

which can be used to train an arbitrary model of the CG energy as follows.

**Teacher-student force-matching.** Our idea is to teach the information about the distribution of the CG coordinates  $\mathbf{r}$  contained in a trained latent-variable model  $\mathcal{V}(\mathbf{r}, \boldsymbol{\eta}; \theta_{\text{flow}})$  to a “student” CG potential  $V(\mathbf{r}; \theta_{\text{pot}})$  that does not suffer from the architectural constraints of flows. We first draw samples

$(\mathbf{r}, \boldsymbol{\eta})$  from our flow model and compute instantaneous forces over CG coordinates  $\mathbf{r}$ :

$$\tilde{\mathbf{f}}(\mathbf{r}, \boldsymbol{\eta}; \theta_{\text{flow}}) = -\nabla_{\mathbf{r}} \mathcal{V}(\mathbf{r}, \boldsymbol{\eta}; \theta_{\text{flow}}). \quad [9]$$

Any given  $\mathbf{r}$  may correspond to different  $\tilde{\mathbf{f}}$ s, but on average they give rise to the unbiased mean force:

$$\mathbf{f}(\mathbf{r}; \theta_{\text{flow}}) = \mathbb{E}_{\boldsymbol{\eta} \sim p(\boldsymbol{\eta}|\mathbf{r}; \theta_{\text{flow}})} [\tilde{\mathbf{f}}(\mathbf{r}, \boldsymbol{\eta}; \theta_{\text{flow}})]. \quad [10]$$

This relation allows us to efficiently train an unconstrained  $V(\mathbf{r}; \theta_{\text{pot}})$  via the variational force-matching objective

$$\mathcal{L}(\theta_{\text{pot}}) = \mathbb{E}_{(\mathbf{r}, \boldsymbol{\eta}) \sim p(\theta_{\text{flow}})} \left[ \left\| \tilde{\mathbf{f}}(\mathbf{r}, \boldsymbol{\eta}; \theta_{\text{flow}}) + \nabla_{\mathbf{r}} V(\mathbf{r}; \theta_{\text{pot}}) \right\|_2^2 \right]. \quad [11]$$

As shown in the supplementary information (SI), the gradients of Eq. (11) with respect to  $\theta_{\text{pot}}$  provides an unbiased estimator that does not depend on  $\theta_{\text{flow}}$ . The proposed approach resembles conventional force matching for coarse graining, but with the difference that it averages over fewer degrees  $\boldsymbol{\eta}$  rather than a larger amount of (mainly solvent) degrees of freedom.

As will be shown in the Results, the student model can mitigate flaws in the flow models, namely samples that deviate from physics laws (e.g., containing steric clashes) and the ruggedness of the CG energy surface. The student model is also regularized to entail a more robust CG potential than the direct force output of the flow for molecular dynamics simulation. In addition, the flexibility in choosing the functional form of the CG energy function allows built-in symmetries such as roto-translational energy invariance (20) and parameter sharing for obtaining a transferable force field (22).

Fitting potential models on data by using approximating force information is routinely used in the machine learning community under the term *score matching* (45–48). Such work focuses on minimizing the implicit score matching objective as defined in Ref. (45), e.g., using denoising score matching (46) or noisy approximations of the potential Laplacian (47). Yet, to the best of our knowledge, no such prior work considered explicit force-matching against a reference model which had been fitted using a likelihood-based objective.

## Results

We now employ the flow-matching method to obtain coarse-grained molecular models of small proteins. To this end, we train flows on the CG coordinate samples extracted from all-atom simulation trajectories. Trained flow models can generate CG coordinates and accompanying forces, which in turn are used to train a neural CG potential via force matching. For demonstration purposes, this work uses an improved version of the CGnet architecture (20) to represent the CG force field (see Methods). Therefore, these secondary CG models will be denoted as “Flow-CGnets”.

**Flow-matching learns accurate CG force fields.** As a first example, we consider capped alanine, also known as alanine dipeptide, to demonstrate that flow-matching can learn accurate CG force fields and achieve much higher statistical efficiency than force matching. As in previous work (20, 22), the CG mapping is defined as slicing out the coordinates of five backbone carbons and nitrogens (Fig. 2a).

We quantify the accuracy of different methods based on equilibrium statistics from either direct sampling (for flows)

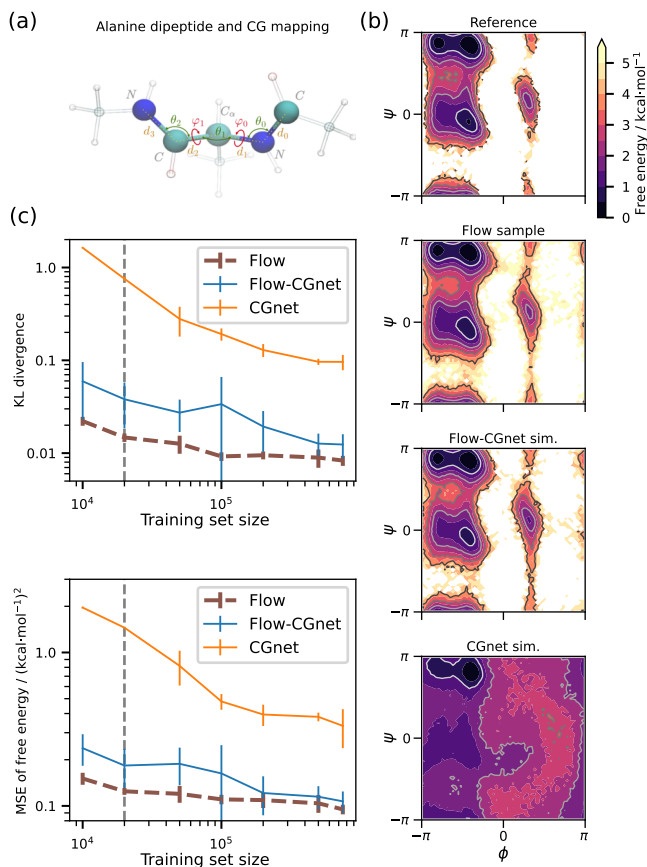


**Fig. 2.** Application of flow-matching on capped alanine. **a)** The CG mapping used for the flow and CGnets,  $\varphi_0, \varphi_1$  represents main chain torsion angles  $\phi$  and  $\psi$ , respectively. **b)** Free energy profile of capped alanine projected on the  $\phi/\psi$  plane (Ramachandran plot) for the all-atom ground truth from MD simulation (ground truth), for the flow model, for the Flow-CGnet and for original CGnet model (baseline). The latter three were trained against 20,000 data points from the reference data (indicated by the vertical grey dashed lines in **(c)**). **c)** Model accuracy as a function of training set size for capped alanine. Shown metrics are estimated KL divergence and MSE between discrete free energies on the  $\phi/\psi$  plane. Brown dashed curves correspond to the flow after MLE training, while solid lines show values for the CGNets trained on either the flow sample (blue) or the all-atom ground truth sample (orange).

or long simulation trajectories (for CGnets). We focus on the joint distributions of the  $\phi$ - and  $\psi$ -dihedral angles along the backbone (i.e., Ramachandran plot, Fig. 2b), which are the main degrees of freedom for this system (49). The ground truth for comparison comes from all-atom MD simulation (2 microseconds in total, see Methods). As for baseline, we use CGnets trained with classical force matching (20, 27) employing forces stored during all-atom simulations. As illustrated by Fig. 2b, the flow and Flow-CGnet can recover the reference distribution to a very good approximation when 20,000 reference conformations are used. In contrast, a normal CGnet cannot effectively model the dihedral free energy in this low data regime, even with the additionally available force information: the free energy minima are more or less located according to the ground truth, but the dihedral distribution smears over the whole space. This comparison displays the advantage of the flow-matching method, which infers the boundary of energy basins as well as relative weighting between different metastable states better than force-matching, especially for regions rarely covered by the training data, e.g., at transition

states.

### Flow-matching is more data efficient than force-matching.

The better accuracy of Flow-CGnet models can be attributed to higher statistical efficiency. For illustration, we measure the effects of the training set size on the KL divergence and mean square error of torsional free energy, which are computed on a discrete histogram against the validation data distribution (22). Concretely, we perform training with a varying number of samples in the training set for both flow-matching and baseline force-matching. Detailed training setup can be found in SI.

It can be observed that the direct samples from the flow model ranks first regarding both criteria (Fig. 2c), which renders the knowledge transfer to a student Flow-CGnet model to be “lossy”. Nevertheless, the secondary model provides a potential that is not only faster to evaluate, but also numerically more stable for CG molecular dynamics. Despite that the flow model automatically provides a differentiable energy function, it is not fully accurate in regions with low Boltzmann probabilities: a simulation with flow potential often visits spurious states outside of the distribution and sometimes experiences numerical blow-ups on the boundary of training data distribution. This issue is solved by our two-stage training strategy, in which the CGnet can incorporate an additive, physics-inspired term (i.e., the prior energy) to set simulation-friendly energy barriers and rule out outlier conformations (20). Flow samples with unrealistically high force magnitude or located in unrealistic conformational regions can be filtered or reweighted before feeding to the CGnet training (see Methods and SI). The remaining samples mostly lie in the high-probability region, thus bringing informative forces for force-matching training. As a result, the Flow-CGnet also benefits from the flow’s efficiency: it achieves an equivalent performance of CGnet at full data set size even with the smallest tested input data amount (Fig. 2c).

Putting the pieces together, here we offer an explanation for the higher data efficiency of Flow-CGnet. The flow can effectively approximate a Boltzmann distribution with relatively few observed conformations. Although its free energy surface is not necessarily well behaved in local details, the flow can generate abundant samples and forces according to the learned distribution. Additionally, the augmentation channels in the flow model are much fewer in number and have simpler distribution than the internal degrees of freedom in the all-atom system, and therefore the flow’s sample forces have much less noise than instantaneous forces stored in all-atom simulations, and better represent the CG mean force. In this sense, when a proper sample filtering scheme and regularizations on the CGnet models are adopted, the flow can become superior to a limited set of all-atom data in terms of the number of samples as well as the signal-to-noise ratio of forces it feeds to the secondary CGnet. The performance in this test case suggests Flow-CGnets may extend the application of neural CG potentials to more complex macromolecular systems, where usually only a limited amount of conformations and no forces are available.

**Flow-matching of fast-folding proteins.** The flow-matching method is applied to molecular trajectories of four small proteins from Ref. (5). We consider four proteins, namely chignolin, tryptophan cage (trpcage), the  $\alpha/\beta$  protein BBA (bba), and the villin headpiece (villin) that consist of 10, 20,

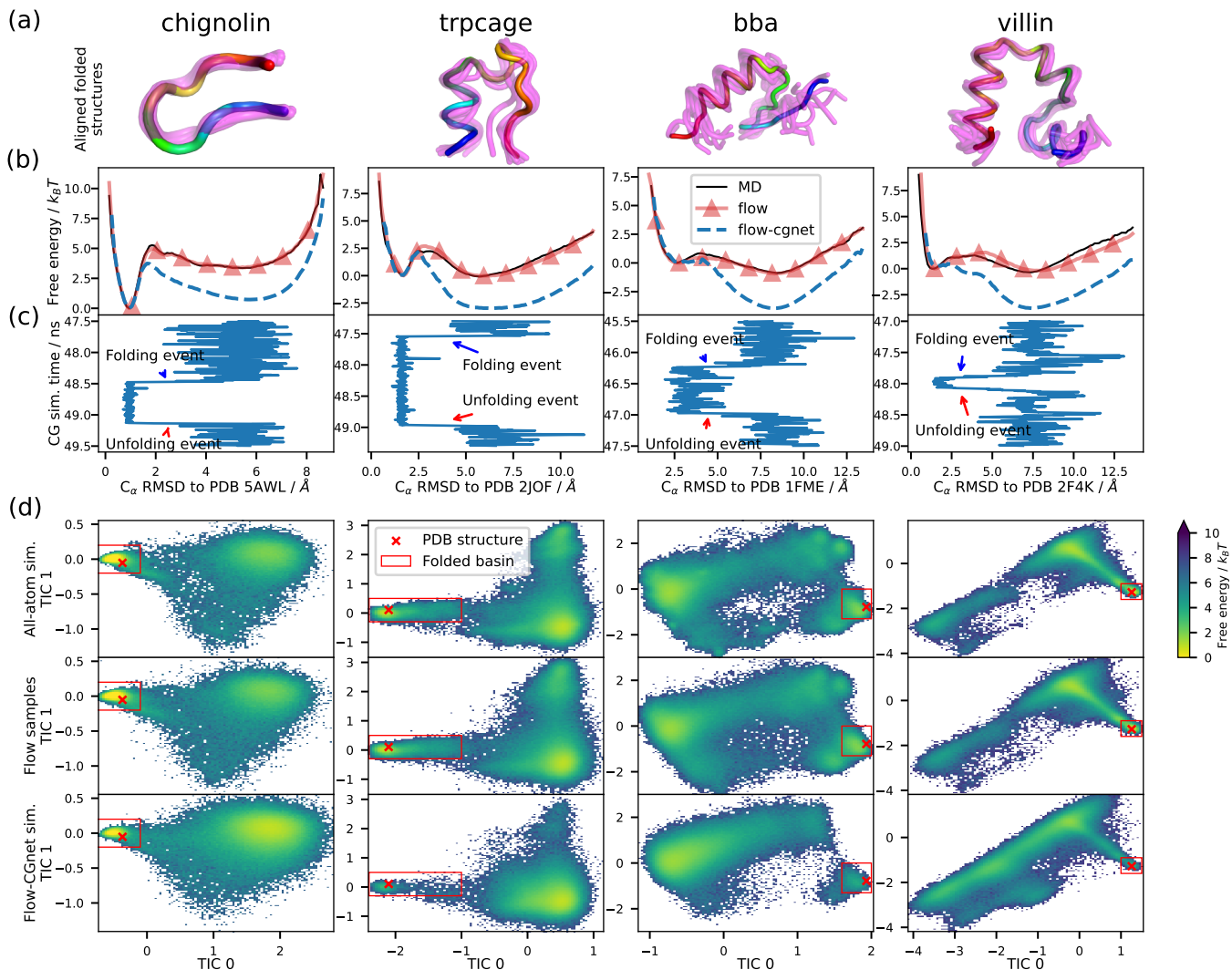


**Fig. 3.** Flow-matching results for four fast-folding proteins. From top to bottom: **a)** 10 exemplary folded samples from CG simulation (shown in half-transparent magenta) superposed on the experimental structure (rainbow color scheme). **b)** free energy curve over RMSD for the MD, flow and Flow-CGnet samples with PDB structure as the reference; **c)** RMSD time series excerpt from CG simulation showing folding and unfolding events; **d)** free energy landscapes of all-atom MD, flow and Flow-CGnet model over TICs, red crosses, and rectangles denoting experimental structures and folded state according to MD trajectories, respectively;

28, and 35 amino acids, respectively (see Ref. (5) for simulation details). These small proteins can be modeled by a flow that operates fully in internal coordinates. As for other fast folding proteins in Ref. (5), some only have a marginally stable state that closely resembles the PDB structure throughout the all-atom trajectories, e.g., BBL; for some fast folders, we can acquire reasonable good flow models, but the folded state cannot be stabilized by the subsequent Flow-CGnet models, e.g., wwdomain and homeodomain; for the rest, the internal-coordinate-based flow model cannot effectively capture the full free energy surface (see Discussion section on scalability). Each trajectory corresponds to at least 100  $\mu$ s of all-atom MD. Note that the trajectories do not contain atomistic forces, so force-matching is not an option for parametrizing a CG force field based on these data. Relative entropy minimization is difficult because it would require iteratively re-sampling the CG model during training, introducing excessive computational cost.

All four proteins are coarse-grained using one bead per

residue placed upon the alpha carbon (Fig. 1d). First, normalizing flows are trained for each protein using likelihood maximization on the  $C_\alpha$  coordinates. Second, synthetic position/force pairs are generated by the flow, of which the outliers are filtered and reweighted according to the extent they exceed the force magnitude boundary and violate the minimum pairwise distances, respectively. Last, the protein-specific CGnets are optimized via force-matching on the processed flow samples. The final CGnets are simulated using Langevin dynamics with parallel tempering to produce equilibrium samples from the CG model. The trajectories from the replica at the same temperature as the all-atom simulation are used for the analyses below. In order to show folding and unfolding events occur without enhanced sampling strategies, we also performed pure Langevin dynamics simulations with learned Flow-CGnet models. The details on the procedure of training and simulation as well as hyperparameter choices can be found in Methods and SI.

**Flow-CGnets recover native structures.** Figure 3 compares protein folding between the atomistic and CG simulations. All CG models recover the folded PDB structures up to 2.5 Å RMSD, which is of similar quality as the reference all-atom simulations. Figure 3a shows representative structures from the CG simulations superposed with the experimental crystal structures, demonstrating excellent agreement. The free energy plots over the RMSD (Fig. 3b) indicate that the CG conformational distribution matches the projected all-atom trajectory for the folded basin: the free energy valleys with the lowest RMSD values are centered around almost the same RMSD value and have nearly indistinguishable widths between the CG and MD densities, which indicates that all CG models accurately represent the flexibility of their respective folded states.

**Flow-CGnets match the folding thermodynamics qualitatively.** Moving into the unfolded region ( $\text{RMSD} \geq 5\text{Å}$  in Fig. 3b), the match between atomistic and CG free energies deteriorates. While all CG models exhibit the characteristic folding energy barrier, the height of this barrier and the folded/unfolded ratio differ between the MD and CG data. Generally, the folded states are less stable in the CG model. While the flow differs by less than  $\approx 1 kT$  from the all-atom result, the Flow-CGnet underestimates the folding free energy by up to  $3 kT$ .

Nevertheless, frequent transitions between folded and unfolded configurations were observed in 50 ns simulation runs without parallel tempering (Fig. 3c). This assures that the models still keep the two states kinetically connected.

**Flow-CGnets approximate folding intermediates and pathways.** Figure 3d show the joint densities over the first two TICA coordinates (50–52) (see SI for TICA details). These reaction coordinates visualize the slowest processes in the MD simulation, which correspond to folding and unfolding, see SI for details. The Flow-CGnet densities resemble the atomistic densities, showing that the global patterns in the folding process are captured. The match deteriorates with increasing sequence length: for chignolin the Flow-CGnet recovers the shape of the distribution well, for trpcage and bba some minor metastable states are missing, and for villin some regions that are sparsely populated in the MD data are overstabilized.

## Discussion

**Training data requirements.** Flow matching does not require the forces to be saved with the simulation data, and is thus more readily applicable than force matching. We have also shown that matching the empirical distribution benefits data efficiency. A drawback is that flow matching requires the underlying all-atom data to come from an equilibrated ensemble. However, this does not need to be achieved in long simulation trajectories: reweighting from biased ensembles, such as replica-exchange simulations, or reweighting of short trajectories via Markov state models (3, 4) are possible.

There are also theoretical developments in generalizing the force-matching method for non-equilibrium cases, such as Ref. (53). In such situations (but generally whenever atomistic force information is available), it might be beneficial to train the flow by combining density estimation with force-matching. Such a mixed loss can be especially efficient when using flows with continuous forces (54).

**Architectural choices for neural networks.** The teacher neural network needs to: (i) be trainable via (approximate) likelihood on sampling data, (ii) permit efficient sampling, and (iii) allow us to compute the instantaneous forces (Eq. (9)). We found that smooth mixture flows (54) on the internal coordinates are able to reproduce the CG conformational distribution very accurately. Other latent variable models, including different normalizing flow architectures as well as variational autoencoders (55) and their generalizations (39, 56), could be used as well. Examples of other generative networks used in coarse-graining applications can be found in Refs. (24, 57, 58).

The student neural network is trained to represent the CG energy. While here we used a modified version of the simple CGnet method (20), this network could be replaced by more advanced neural network architectures, such as SchNet (59) or other graph neural networks (22, 60–66). In particular, in order to train a transferable CG potential, one may train separate system-specific teacher networks (e.g., flows) and use a shared graph-neural network to gain a unified representation of the CG energy.

**Scalability to larger molecules.** We observed that the CG model quality deteriorated and eventually became unusable for larger proteins. This is because the present normalizing flows are built on a global internal coordinate representation. As the length of the peptide chain grows, the target potential energy becomes extremely sensitive with respect to these internal coordinates. For example, a tiny rotation of one torsion can easily cause steric clashes in a different part of the molecule. Applying flow-matching to larger molecules will likely require different featurizations. Other work (32–34, 37, 38) has also found suitable flow architectures for small molecules, proteins, and even explicitly solvated systems, but did not report whether they could produce quantitatively matching forces. There is currently no one-size-fits-all flow method for general molecular applications. Applying the flow-matching method to large biomolecules or crowded molecular systems such as CG fluids or lipids thus likely requires further progress on generative models.

## Conclusions

We have developed a two-stage approach to bottom-up coarse-graining that addresses two major problems with classical approaches, namely data availability and efficiency. The *flow-matching* method produces thermodynamically consistent CG models without relying on either all-atom ground truth forces or subsequent CG simulations. The key ingredient of our method is a generative deep neural network that is introduced into the optimization workflow. Compared with classical force-matching, flow-matching captures the global thermodynamics of small peptides much more accurately than CGnet models trained with force matching. Interestingly, this was even the case, when only a fraction ( $< 10\%$ ) of the data was used during training. Applications to four small proteins yielded CG potentials that were able to fold and unfold the proteins via the same pathways as all-atom MD. Thereby, the present work opens a new and efficient path to reach near-atomistic accuracy on scales not amenable to atomistic simulations. The method will directly benefit from the currently rapid development of more powerful generative networks and deep CG potentials to systematically bridge atomistic and mesoscopic scales.

## Materials and Methods

We describe how we can use and evaluate this approach when modeling the CG potential of given protein systems.

**Models.** As a first step, we have to decide how we choose our CG coordinates. In the second step, we need to design a suitable flow transformation  $\Phi(\cdot; \theta_{\text{flow}})$  for the density estimation part. Finally, we need to choose an unconstrained model  $V(\mathbf{r}; \theta_{\text{pot}})$  that we can train against the forces of the flow-induced potential  $\mathcal{V}(\mathbf{r}, \boldsymbol{\eta}; \theta_{\text{flow}})$ .

**Coarse-graining operator  $\Xi$ .** Our coarse-graining operator  $\Xi: \mathbb{R}^{3N} \rightarrow \mathbb{R}^{3n}$  projects an  $N$ -atom peptide conformation onto a subset of  $n$  of its backbone atoms. For smaller systems (e.g., capped alanine) we can choose backbone carbons and nitrogens. For larger systems (e.g., fast-folder proteins) we project all-atom conformations onto  $C_\alpha$  beads of the backbone (see Fig. 1f). Other choices of CG mapping that can be described by a linear operator  $\Xi$ , such as placing a bead on the center of mass for a group of atoms, are also compatible with our methods.

**Flow potential  $\mathcal{V}(\mathbf{r}, \boldsymbol{\eta}; \theta_{\text{flow}})$ .** The inverse flow transformation  $\Phi^{-1}(\cdot; \theta_{\text{flow}})$  required to define  $\mathcal{V}(\mathbf{r}, \boldsymbol{\eta}; \theta_{\text{flow}})$  in Eq. (5) is composed by a fixed coordinate transformation into an internal coordinate (IC) representation followed by a trainable normalizing flow (see Fig. 1d). For the IC transformation, we follow Ref. (32) and project the Cartesian coarse-grained degrees of freedom onto bond lengths, angles, and dihedral torsions of adjacent CG beads. The normalizing flow follows the architecture in Ref. (54) and consists of coupling layers (67, 68) where we transform bonds and angles and torsions using either spline or smooth hypertoric transforms (54, 69). We increase expressivity and relax bijectivity constraints of the normalizing flow by introducing  $k$  additional latent variables  $\boldsymbol{\eta}$  leading to the variational objective Eq. (7). We choose a factorized base density  $q(\mathbf{z}_0, \mathbf{z}_1) = q(\mathbf{z}_0) \cdot q(\mathbf{z}_1)$  given by a uniform density  $q(\mathbf{z}_0) = \mathcal{U}(0, 1)$  for the IC degrees of freedom and an isotropic normal density  $q(\mathbf{z}_1) = \mathcal{N}(0, 1)$  for the latent variables  $\boldsymbol{\eta}$ . Finally, we choose the variational density  $\tilde{\nu}(\boldsymbol{\eta}|\mathbf{r}) = \tilde{\nu}(\boldsymbol{\eta}) = \mathcal{N}(0, 1)$  to be an independent isotropic Gaussian, as well. Additional technical details on the implementation of the normalizing flow can be found in the SI.

**Unconstrained CG potential  $V(\mathbf{r}; \theta_{\text{pot}})$ .** The unconstrained potential  $V(\mathbf{r}; \theta_{\text{pot}})$  in the second step follows the *CGnet* architecture in Ref. (20). This model transforms Euclidean coordinates of the CG beads into pairwise distances, angles and torsions (similar to the IC transformation introduced in the last paragraph). Then these features are fed into a fully connected neural network to output a scalar energy. Furthermore, the model adds simple repulsive and harmonic *prior energy* terms to this scalar, which prevent steric clashes and bond breaking (see Fig. 1e). We extended the original architecture by introducing skip-connections (70) and replaced **tanh**-activations with **silu**-activations (71) which both greatly improved results. Technical details on the implementation of this coarse-graining potential can be found in the SI.

**Training.** The flow potential can be trained on the trajectory data using the variational bound to the likelihood Eq. (7). During training, we monitor the validation likelihood. We stop training once we observe convergence and pick the checkpoint with the highest validation log-likelihood for later use.

Due to the constraints of a normalizing flow, some of the generated samples from the teacher model are not perfect. For example, a small number of samples come with significantly larger force magnitudes than the rest of the samples and can disrupt the force-matching training of the *CGnet*. We solve this with a rejection sampling scheme and filter flow samples with a set threshold on force magnitude. Additionally, there are flow samples that contain non-neighboring pairs with shorter distances than the minimum observed in the ground truth, to which lower weights are assigned via a free energy perturbation scheme.

The unconstrained potential is then trained against the processed flow samples using the variational force-matching objective Eq. (11). Detailed setup and explanation of the training can be found in the SI.

**Coarse-grained sampling.** For the flow models, we draw independent samples in latent space according to the prior distributions and use the forward transformation of the flow to map them to CG coordinates. As for the *CGnet*-based models, we perform MD simulations in the CG space, similarly as in Refs. (20) and (22) (Except for the time step (5-fs for capped alanine and 2-fs for fast folding proteins), we keep the simulation parameters, such as the thermostat temperature and friction coefficient, consistent with the reference all-atom simulations. Note that there is no simple correspondence between the CG kinetics and thus timescale and the all-atom system (19).

In addition, two methods are used to facilitate sampling: batched simulations from different starting structures and parallel tempering. The starting structures are sampled according to the equilibrium distribution of the all-atom simulations (following Ref. (20)). The parallel tempering employs two replicas at temperatures 300 K and 450 K for CG alanine and three replicas at temperatures  $T_0$ ,  $\sqrt{T_0 \times 500 \text{ K}}$  and 500 K for fast folders, in which  $T_0$  is the simulation temperature used for the reference all-atom data set (see Ref. (5)). The conformations at the reference temperature are recorded every 100 or 250 time steps for CG alanine and fast folding proteins, respectively. Other aspects of conducting the simulations can be found in SI.

**ACKNOWLEDGMENTS.** The authors would like to thank Aleksander E. P. Durumeric, Nicholas E. Charron, Brooke E. Husic, Manuel Dibak, Leon Klein, Michele Invernizzi and Leon Sixt for insightful discussions. We gratefully acknowledge funding from European Commission (Grant No. ERC CoG 772230 “ScaleCell”), the International Max Planck Research School for Biology and Computation (IMPRS-BAC), the BMBF (Berlin Institute for Learning and Data, BIFOLD), the Berlin Mathematics center MATH+ (AA1-6, EF1-2) and the Deutsche Forschungsgemeinschaft DFG (GRK DAEDALUS, SFB1114/A04 and B08). C.C. acknowledges funding from the Deutsche Forschungsgemeinschaft DFG (SFB/TRR 186, Project A12; SFB 1114, Projects B03 and A04; SFB 1078, Project C7; and RTG 2433, Project Q05), the National Science Foundation (CHE-1738990, CHE-1900374, and PHY-2019745), and the Einstein Foundation Berlin (Project 0420815101). The 3D molecular structures are visualized with PyMOL (72).

1. DE Shaw, et al., Anton 2: Raising the Bar for Performance and Programmability in a Special-Purpose Molecular Dynamics Supercomputer. *Int. Conf. High Perform. Comput. Networking, Storage Anal. SC 2015-January*, 41–53 (2014).
2. DE Shaw, et al., Anton 3: Twenty Microseconds of Molecular Dynamics Simulation before Lunch. *Int. Conf. High Perform. Comput. Networking, Storage Anal. SC (2021)*.
3. JH Prinz, et al., Markov models of molecular kinetics: Generation and validation. *J. Chem. Phys.* **134**, 174105 (2011).
4. BE Husic, VS Pande, Markov state models: From an art to a science. *J. Am. Chem. Soc.* **140**, 2386–2396 (2018).
5. K Lindorff-Larsen, S Piana, RO Dror, DE Shaw, How fast-folding proteins fold. *Science* **334**, 517–520 (2011).
6. N Plattner, S Doerr, G De Fabritiis, F Noé, Complete protein-protein association kinetics in atomic detail revealed by molecular dynamics simulations and Markov modelling. *Nat. Chem.* **2017 910 9**, 1005–1011 (2017).
7. C Clementi, H Nymeyer, JN Onuchic, Topological and energetic factors: what determines the structural details of the transition state ensemble and “en-route” intermediates for protein folding? an investigation for small globular proteins. *J. Mol. Biol.* **298**, 937–953 (2000).
8. C Clementi, Coarse-grained models of protein folding: Toy-models or predictive tools? *Curr. Opin. Struct. Biol.* **18**, 10–15 (2008).
9. S Matysiak, C Clementi, Optimal combination of theory and experiment for the characterization of the protein folding landscape of S6: How far can a minimalist model go? *J. Mol. Biol.* **343**, 235–248 (2004).
10. S Matysiak, C Clementi, Minimalist Protein Model as a Diagnostic Tool for Misfolding and Aggregation. *J. Mol. Biol.* **363**, 297–308 (2006).
11. P Das, S Matysiak, C Clementi, Balancing energy and entropy: A minimalist model for the characterization of protein folding landscapes. *Proc. Natl. Acad. Sci. USA* **102**, 10141–10146 (2005).
12. MG Saunders, GA Voith, Coarse-Graining Methods for Computational Biology. *Annu. Rev. Bioph. Biom.* **42**, 73–93 (2013).
13. WG Noid, Perspective: Coarse-grained models for biomolecular systems. *J. Chem. Phys.* **139**, 090901 (2013).
14. HI Ingólfsson, et al., The power of coarse graining in biomolecular simulations. *WIREs Comput. Mol. Sci.* **4**, 225–248 (2014).
15. S Kmiecik, et al., Coarse-grained protein models and their applications. *Chem. Rev.* **116**, 7898–7936 (2016).
16. AJ Pak, GA Voith, Advances in coarse-grained modeling of macromolecular complexes. *Curr. Opin. Struct. Biol.* **52**, 119 (2018).



17. J Chen, J Chen, G Pinamonti, C Clementi, Learning effective molecular models from experimental observables. *J. Chem. Theory Comput.* **14**, 3849–3858 (2018).
18. N Singh, W Li, Recent Advances in Coarse-Grained Models for Biomolecules and Their Applications. *Int. J. Mol. Sci.* **20** (2019).
19. F Nüsse, L Boninsegna, C Clementi, Coarse-graining molecular systems by spectral matching. *J. Chem. Phys.* **151**, 044116 (2019).
20. J Wang, et al., Machine learning of coarse-grained molecular dynamics force fields. *ACS central science* **5**, 755–767 (2019).
21. J Wang, S Chmiela, KR Müller, F Noé, C Clementi, Ensemble learning of coarse-grained molecular dynamics force fields with a kernel approach. *J. Chem. Phys.* **152**, 194106 (2020).
22. BE Husic, et al., Coarse graining molecular dynamics with graph neural networks. *The J. Chem. Phys.* **153**, 194101 (2020).
23. L Boninsegna, R Banisch, C Clementi, A data-driven perspective on the hierarchical assembly of molecular structures. *J. Chem. Theory Comput.* **14**, 453–460 (2018).
24. W Wang, R Gómez-Bombarelli, Coarse-graining auto-encoders for molecular dynamics. *npj Comput. Mater.* **5**, 1–9 (2019).
25. D Reith, M Pütz, F Müller-Plathe, Deriving effective mesoscale potentials from atomistic simulations. *J. Comput. Chem.* **24**, 1624–1636 (2003).
26. S Izvekov, GA Voth, A Multiscale Coarse-Graining Method for Biomolecular Systems. *J. Phys. Chem. B* **109**, 2469–2473 (2005).
27. WG Noid, et al., The multiscale coarse-graining method. I. A rigorous bridge between atomistic and coarse-grained models. *J. Chem. Phys.* **128**, 244114 (2008).
28. MS Shell, The relative entropy is fundamental to multiscale and inverse thermodynamic problems. *J. Chem. Phys.* **129**, 144108 (2008).
29. EG Tabak, E Vanden-Eijnden, et al., Density estimation by dual ascent of the log-likelihood. *Commun. Math. Sci.* **8**, 217–233 (2010).
30. D Rezende, S Mohamed, Variational inference with normalizing flows in *International Conference on Machine Learning*. (PMLR), pp. 1530–1538 (2015).
31. G Papamakarios, E Nalisnick, DJ Rezende, S Mohamed, B Lakshminarayanan, Normalizing flows for probabilistic modeling and inference. *J. Mach. Learn. Res.* **22**, 1–64 (2021).
32. F Noé, S Olsson, J Köhler, H Wu, Boltzmann generators: Sampling equilibrium states of many-body systems with deep learning. *Science* **365**, eaaw1147 (2019).
33. M Gabriéu, GM Rotskoff, E Vanden-Eijnden, Adaptive monte carlo augmented with normalizing flows. *Proc. Natl. Acad. Sci. United States Am.* **119** (2022).
34. SH Li, CX Dong, L Zhang, L Wang, Neural Canonical Transformation with Symplectic Flows. *Phys. Rev. X* **10**, 021020 (2020).
35. KA Nicoli, et al., Asymptotically unbiased estimation of physical observables with neural samplers. *Phys. Rev. E* **101**, 023304 (2020).
36. Q Liu, J Xu, R Jiang, WH Wong, Density estimation using deep generative neural networks. *Proc. Natl. Acad. Sci. U. S. A.* **118** (2021).
37. X Ding, B Zhang, DeepBAR: A Fast and Exact Method for Binding Free Energy Computation. *J. Phys. Chem. Lett.* **12**, 2509–2515 (2021).
38. P Wirsberger, et al., Targeted free energy estimation via learned mappings. *The J. Chem. Phys.* **153**, 144112–144112 (2020).
39. H Wu, J Köhler, F Noe, Stochastic normalizing flows in *Advances in Neural Information Processing Systems*, eds. H Larochelle, M Ranzato, R Hadsell, MF Balcan, H Lin. (Curran Associates, Inc.), Vol. 33, pp. 5933–5944 (2020).
40. G Ciccotti, T Lelievre, E Vanden-Eijnden, Projection of diffusions on submanifolds: Application to mean force computation. *Commun. Pure Appl. Math.* **61**, 371–408 (2008).
41. Y LeCun, S Chopra, R Hadsell, M Ranzato, F Huang, Energy-Based Models in *Predicting Structured Data*. (The MIT Press), (2007).
42. CW Huang, L Dinh, A Courville, Augmented normalizing flows: Bridging the gap between generative flows and latent variable models. *arXiv preprint arXiv:2002.07101* (2020).
43. J Chen, C Lu, B Chenil, J Zhu, T Tian, Vflow: More expressive generative flows with variational data augmentation in *International Conference on Machine Learning*. (PMLR), pp. 1660–1669 (2020).
44. R Cornish, A Caterini, G Deligiannidis, A Doucet, Relaxing bijectivity constraints with continuously indexed normalising flows in *International Conference on Machine Learning*. (PMLR), pp. 2133–2143 (2020).
45. A Hyvärinen, P Dayan, Estimation of non-normalized statistical models by score matching. *J. Mach. Learn. Res.* **6** (2005).
46. P Vincent, A connection between score matching and denoising autoencoders. *Neural Comput.* **23**, 1661–1674 (2011).
47. Y Song, S Garg, J Shi, S Ermon, Sliced score matching: A scalable approach to density and score estimation in *Uncertainty in Artificial Intelligence*. (PMLR), pp. 574–584 (2020).
48. Y Song, DP Kingma, How to train your energy-based models. *arXiv preprint arXiv:2101.03288* (2021).
49. DJ Tobias, CL Brooks III, Conformational equilibrium in the alanine dipeptide in the gas phase and aqueous solution: A comparison of theoretical results. *J. Phys. Chem.* **96**, 3864–3870 (1992).
50. Y Naritomi, S Fuchigami, Slow dynamics in protein fluctuations revealed by time-structure based independent component analysis: The case of domain motions. *The J. Chem. Phys.* **134**, 065101 (2011) TICA pioneer 3/3.
51. G Pérez-Hernández, F Paul, T Giorgio, G De Fabritiis, F Noé, Identification of slow molecular order parameters for markov model construction. *J. Chem. Phys.* **139**, 07B604\_1 (2013).
52. CR Schwantes, VS Pande, Improvements in markov state model construction reveal many non-native interactions in the folding of ntl9. *J. Chem. Theory Comput.* **9**, 2000–2009 (2013).
53. V Harmandaris, E Kalligiannaki, M Katsoulakis, P Plecháč, Path-space variational inference for non-equilibrium coarse-grained systems. *J. Comput. Phys.* **314**, 355–383 (2016).
54. J Köhler, A Krämer, F Noé, Smooth normalizing flows in *Advances in Neural Information Processing Systems*. Vol. 34, (2021).
55. DP Kingma, M Welling, Auto-Encoding Variational Bayes in *2nd International Conference on Learning Representations, ICLR 2014, Banff, AB, Canada, April 14-16, 2014, Conference Track Proceedings*. (2014).
56. D Nielsen, P Jaini, E Hoogeboom, O Winther, M Welling, Survae flows: Surjections to bridge the gap between vaes and flows in *Advances in Neural Information Processing Systems*. Vol. 33, (2020).
57. W Wang, et al., Generative Coarse-Graining of Molecular Conformations. *arXiv preprint arXiv:2201.12176* (2022).
58. M Stieffenhofer, M Wand, T Bereau, Adversarial reverse mapping of equilibrated condensed-phase molecular structures. *Mach. Learn. Sci. Technol.* **1**, 045014 (2020).
59. KT Schütt, HE Sauceda, PJ Kindermans, A Tkatchenko, KR Müller, SchNet – A deep learning architecture for molecules and materials. *J. Chem. Phys.* **148**, 241722 (2018).
60. DP Kovács, et al., Linear Atomic Cluster Expansion Force Fields for Organic Molecules: Beyond RMSE. *J. Chem. Theory Comput.* **17**, 7696–7711 (2021).
61. N Thomas, et al., Tensor field networks: Rotation- and translation-equivariant neural networks for 3D point clouds. *arXiv preprint arXiv:1802.08219* (2018).
62. J Klicpera, J Groß, S Günnemann, Directional message passing for molecular graphs in *International Conference on Learning Representations (ICLR)*. (2020).
63. S Batzner, et al., E(3)-Equivariant Graph Neural Networks for Data-Efficient and Accurate Interatomic Potentials. *arXiv preprint arXiv:2101.03164* (2021).
64. OT Unke, M Meuwly, PhysNet: A Neural Network for Predicting Energies, Forces, Dipole Moments, and Partial Charges. *J. Chem. Theory Comput.* **15**, 3678–3693 (2019).
65. JS Smith, O Isayev, AE Roitberg, ANI-1: an extensible neural network potential with DFT accuracy at force field computational cost. *Chem. Sci.* **8**, 3192–3203 (2017).
66. Y Chen, et al., Machine learning implicit solvation for molecular dynamics. *J. Chem. Phys.* **155**, 084101 (2021).
67. L Dinh, D Krueger, Y Bengio, Nice: Non-linear independent components estimation. *arXiv preprint arXiv:1410.8516* (2014).
68. L Dinh, J Sohl-Dickstein, S Bengio, Density estimation using real NVP in *5th International Conference on Learning Representations, ICLR 2017, Toulon, France, April 24-26, 2017, Conference Track Proceedings*. (OpenReview.net), (2017).
69. C Durkan, A Bekasov, I Murray, G Papamakarios, Neural spline flows in *Advances in Neural Information Processing Systems*. pp. 7509–7520 (2019).
70. K He, X Zhang, S Ren, J Sun, Deep residual learning for image recognition in *Proceedings of the IEEE conference on computer vision and pattern recognition*. pp. 770–778 (2016).
71. S Elfving, E Uchibe, K Doya, Sigmoid-weighted linear units for neural network function approximation in reinforcement learning. *Neural networks : official journal Int. Neural Netw. Soc.* **107**, 3–11 (2018).
72. Schrödinger, LLC, The PyMOL molecular graphics system, version 1.8 (2015).
73. R Douc, E Moulines, D Stoffer, *Nonlinear time series: Theory, methods and applications with R examples*. (CRC press), (2014).
74. RW Zwanzig, High-temperature equation of state by a perturbation method. i. nonpolar gases. *J. Chem. Phys.* **22**, 1420–1426 (1954).
75. DJ Rezende, et al., Normalizing flows on tori and spheres in *International Conference on Machine Learning*. (PMLR), pp. 8083–8092 (2020).
76. P Eastman, et al., OpenMM 7: Rapid development of high performance algorithms for molecular dynamics. *PLoS Comput. Biol.* **13**, e1005659 (2017).
77. DP Kingma, J Ba, Adam: A method for stochastic optimization. *arXiv preprint arXiv:1412.6980* (2014).
78. M Hoffmann, et al., Deeptime: a python library for machine learning dynamical models from time series data. *Mach. Learn. Sci. Technol.* **3**, 015009 (2022).

# Supplementary Information

## 1. Proofs and Derivations

**A. Fisher-Identity.** For any sufficiently smooth probability density  $p(\mathbf{r}, \boldsymbol{\eta})$  on  $\mathbb{R}^d$  we have the *Fisher-identity* (73):

**Lemma 1.**

$$\nabla_{\mathbf{x}} \log p(\mathbf{x}) = \mathbb{E}_{\mathbf{y} \sim p(\mathbf{y}|\mathbf{x})} [\nabla_{\mathbf{x}} \log p(\mathbf{x}|\mathbf{y})]. \quad [12]$$

*Proof.*

$$\nabla_{\mathbf{x}} \log p(\mathbf{x}) = \frac{1}{p(\mathbf{x})} \nabla_{\mathbf{x}} p(\mathbf{x}) \quad [13]$$

$$= \frac{1}{p(\mathbf{x})} \nabla_{\mathbf{x}} \int d\mathbf{y} p(\mathbf{x}, \mathbf{y}) \quad [14]$$

$$= \frac{1}{p(\mathbf{x})} \int d\mathbf{y} \nabla_{\mathbf{x}} p(\mathbf{x}, \mathbf{y}) \quad [15]$$

$$= \frac{1}{p(\mathbf{x})} \int d\mathbf{y} p(\mathbf{x}, \mathbf{y}) \nabla_{\mathbf{x}} \log p(\mathbf{x}, \mathbf{y}) \quad [16]$$

$$= \int d\mathbf{y} \frac{p(\mathbf{y}, \mathbf{x})}{p(\mathbf{x})} \left[ \nabla_{\mathbf{x}} \log p(\mathbf{x}|\mathbf{y}) + \underbrace{\nabla_{\mathbf{x}} \log p(\mathbf{y})}_{=0} \right] \quad [17]$$

$$= \int d\mathbf{y} p(\mathbf{y}|\mathbf{x}) \nabla_{\mathbf{x}} \log p(\mathbf{x}|\mathbf{y}) \quad [18]$$

$$= \mathbb{E}_{\mathbf{y} \sim p(\mathbf{y}|\mathbf{x})} [\nabla_{\mathbf{x}} \log p(\mathbf{x}|\mathbf{y})]. \quad [19]$$

□

**B. Variational bound on the likelihood of the latent-variable model.**

$$\mathcal{L}(\boldsymbol{\theta}_{\text{flow}}) = \mathbb{E}_{\mathbf{r} \sim \mathcal{D}, \boldsymbol{\eta} \sim \tilde{p}(\boldsymbol{\eta}|\mathbf{r})} [-\log p(\mathbf{r}, \boldsymbol{\eta}; \boldsymbol{\theta}_{\text{flow}})] \quad [20]$$

$$= -\frac{1}{|\mathcal{D}|} \sum_{\mathbf{r} \in \mathcal{D}} \int d\boldsymbol{\eta} \tilde{p}(\boldsymbol{\eta}|\mathbf{r}) \log p(\mathbf{r}, \boldsymbol{\eta}; \boldsymbol{\theta}_{\text{flow}}) \quad [21]$$

$$= -\frac{1}{|\mathcal{D}|} \sum_{\mathbf{r} \in \mathcal{D}} \int d\boldsymbol{\eta} \tilde{p}(\boldsymbol{\eta}|\mathbf{r}) (\log p(\mathbf{r}; \boldsymbol{\theta}_{\text{flow}}) + \log p(\boldsymbol{\eta}|\mathbf{r}; \boldsymbol{\theta}_{\text{flow}})) \quad [22]$$

$$= -\frac{1}{|\mathcal{D}|} \sum_{\mathbf{r} \in \mathcal{D}} \int d\boldsymbol{\eta} \tilde{p}(\boldsymbol{\eta}|\mathbf{r}) \log p(\mathbf{r}; \boldsymbol{\theta}_{\text{flow}}) - \frac{1}{|\mathcal{D}|} \sum_{\mathbf{r} \in \mathcal{D}} \int d\boldsymbol{\eta} \tilde{p}(\boldsymbol{\eta}|\mathbf{r}) \log p(\boldsymbol{\eta}|\mathbf{r}; \boldsymbol{\theta}_{\text{flow}}) \quad [23]$$

$$= -\frac{1}{|\mathcal{D}|} \sum_{\mathbf{r} \in \mathcal{D}} \log p(\mathbf{r}; \boldsymbol{\theta}_{\text{flow}}) + \mathbb{E}_{\mathbf{r} \sim \mathcal{D}} [H[\tilde{p}(\cdot|\mathbf{r}), p(\cdot|\mathbf{r}; \boldsymbol{\theta}_{\text{flow}})]] \quad [24]$$

$$= \mathbb{E}_{\mathbf{r} \sim \mathcal{D}} [-\log p(\mathbf{r}; \boldsymbol{\theta}_{\text{flow}})] + \mathbb{E}_{\mathbf{r} \sim \mathcal{D}} \left[ \underbrace{H[\tilde{p}(\cdot|\mathbf{r}), p(\cdot|\mathbf{r}; \boldsymbol{\theta}_{\text{flow}})]}_{\geq 0} \right] \quad [25]$$

$$\geq \mathbb{E}_{\mathbf{r} \sim \mathcal{D}} [-\log p(\mathbf{r}; \boldsymbol{\theta}_{\text{flow}})] \quad [26]$$

where  $H(\cdot, \cdot)$  denotes the cross-entropy.

**C. Consistency of teacher-student force-matching.** We first note that

$$\mathbf{f}(\mathbf{r}, \boldsymbol{\eta}; \boldsymbol{\theta}_{\text{flow}}) = \nabla_{\mathbf{r}} \log p(\mathbf{r}, \boldsymbol{\eta}; \boldsymbol{\theta}_{\text{flow}}) \quad [27]$$

$$= \nabla_{\mathbf{r}} \log p(\mathbf{r}|\boldsymbol{\eta}; \boldsymbol{\theta}_{\text{flow}}) + \nabla_{\mathbf{r}} \log p(\boldsymbol{\eta}; \boldsymbol{\theta}_{\text{flow}}) \quad [28]$$

$$= \nabla_{\mathbf{r}} \log p(\mathbf{r}|\boldsymbol{\eta}; \boldsymbol{\theta}_{\text{flow}}). \quad [29]$$

Combining Jensen's inequality with Lemma 1, we obtain

$$\mathcal{L}(\boldsymbol{\theta}_{\text{pot}}) = \mathbb{E}_{(\mathbf{r}, \boldsymbol{\eta}) \sim p(\mathbf{r}, \boldsymbol{\eta}; \boldsymbol{\theta}_{\text{flow}})} \left[ \|\nabla_{\mathbf{r}} V(\mathbf{r}; \boldsymbol{\theta}_{\text{pot}}) + \mathbf{f}(\mathbf{r}, \boldsymbol{\eta}; \boldsymbol{\theta}_{\text{flow}})\|_2^2 \right] \quad [30]$$

$$= \mathbb{E}_{(\mathbf{r}, \boldsymbol{\eta}) \sim p(\mathbf{r}, \boldsymbol{\eta}; \boldsymbol{\theta}_{\text{flow}})} \left[ \|\nabla_{\mathbf{r}} V(\mathbf{r}; \boldsymbol{\theta}_{\text{pot}}) + \nabla_{\mathbf{r}} \log p(\mathbf{r}|\boldsymbol{\eta}; \boldsymbol{\theta}_{\text{flow}})\|_2^2 \right] \quad [31]$$

$$= \mathbb{E}_{\mathbf{r} \sim p(\mathbf{r}; \boldsymbol{\theta}_{\text{flow}})} \left[ \mathbb{E}_{\boldsymbol{\eta} \sim p(\boldsymbol{\eta}|\mathbf{r}; \boldsymbol{\theta}_{\text{flow}})} \left[ \|\nabla_{\mathbf{r}} V(\mathbf{r}; \boldsymbol{\theta}_{\text{pot}}) + \nabla_{\mathbf{r}} \log p(\mathbf{r}|\boldsymbol{\eta}; \boldsymbol{\theta}_{\text{flow}})\|_2^2 \right] \right] \quad [32]$$

$$\geq \mathbb{E}_{\mathbf{r} \sim p(\mathbf{r}; \boldsymbol{\theta}_{\text{flow}})} \left[ \left\| \nabla_{\mathbf{r}} V(\mathbf{r}; \boldsymbol{\theta}_{\text{pot}}) + \mathbb{E}_{\boldsymbol{\eta} \sim p(\boldsymbol{\eta}|\mathbf{r}; \boldsymbol{\theta}_{\text{flow}})} [\nabla_{\mathbf{r}} \log p(\mathbf{r}|\boldsymbol{\eta}; \boldsymbol{\theta}_{\text{flow}})] \right\|_2^2 \right] \quad [33]$$

$$= \mathbb{E}_{\mathbf{r} \sim p(\mathbf{r}; \boldsymbol{\theta}_{\text{flow}})} \left[ \|\nabla_{\mathbf{r}} V(\mathbf{r}; \boldsymbol{\theta}_{\text{pot}}) + \nabla_{\mathbf{r}} \log p(\mathbf{r}; \boldsymbol{\theta}_{\text{flow}})\|_2^2 \right] \quad [34]$$

$$= \mathbb{E}_{\mathbf{r} \sim p(\mathbf{r}; \boldsymbol{\theta}_{\text{flow}})} \left[ \|\nabla_{\mathbf{r}} V(\mathbf{r}; \boldsymbol{\theta}_{\text{pot}}) + \mathbf{f}(\mathbf{r}; \boldsymbol{\theta}_{\text{flow}})\|_2^2 \right]. \quad [35]$$

Furthermore, we have

$$\mathbb{E}_{(\mathbf{r}, \boldsymbol{\eta}) \sim p(\mathbf{r}, \boldsymbol{\eta}; \boldsymbol{\theta}_{\text{flow}})} \left[ \nabla_{\mathbf{r}} V(\mathbf{r}; \boldsymbol{\theta}_{\text{pot}})^T \mathbf{f}(\mathbf{r}, \boldsymbol{\eta}; \boldsymbol{\theta}_{\text{flow}}) \right] = \mathbb{E}_{\mathbf{r} \sim p(\mathbf{r}; \boldsymbol{\theta}_{\text{flow}})} \left[ \nabla_{\mathbf{r}} V(\mathbf{r}; \boldsymbol{\theta}_{\text{pot}})^T \mathbf{f}(\mathbf{r}; \boldsymbol{\theta}_{\text{flow}}) \right]. \quad [36]$$

From which we can derive

$$\mathbb{E}_{(\mathbf{r}, \boldsymbol{\eta}) \sim p(\mathbf{r}, \boldsymbol{\eta}; \boldsymbol{\theta}_{\text{flow}})} \left[ \|\nabla_{\mathbf{r}} V(\mathbf{r}; \boldsymbol{\theta}_{\text{pot}}) + \mathbf{f}(\mathbf{r}, \boldsymbol{\eta}; \boldsymbol{\theta}_{\text{flow}})\|_2^2 \right] - \mathbb{E}_{\mathbf{r} \sim p(\mathbf{r}; \boldsymbol{\theta}_{\text{flow}})} \left[ \|\nabla_{\mathbf{r}} V(\mathbf{r}; \boldsymbol{\theta}_{\text{pot}}) + \mathbf{f}(\mathbf{r}; \boldsymbol{\theta}_{\text{flow}})\|_2^2 \right] \quad [37]$$

$$= \mathbb{E}_{(\mathbf{r}, \boldsymbol{\eta}) \sim p(\mathbf{r}, \boldsymbol{\eta}; \boldsymbol{\theta}_{\text{flow}})} \left[ \|\mathbf{f}(\mathbf{r}, \boldsymbol{\eta}; \boldsymbol{\theta}_{\text{flow}})\|_2^2 - \|\mathbf{f}(\mathbf{r}; \boldsymbol{\theta}_{\text{flow}})\|_2^2 \right]. \quad [38]$$

Thus, the variational gap introduced by the latent variables does not depend on  $\boldsymbol{\theta}_{\text{pot}}$  which makes

$$\mathbb{E}_{(\mathbf{r}, \boldsymbol{\eta}) \sim p(\mathbf{r}, \boldsymbol{\eta}; \boldsymbol{\theta}_{\text{flow}})} \left[ \nabla_{\boldsymbol{\theta}_{\text{pot}}} \|\nabla_{\mathbf{r}} V(\mathbf{r}; \boldsymbol{\theta}_{\text{pot}}) + \mathbf{f}(\mathbf{r}, \boldsymbol{\eta}; \boldsymbol{\theta}_{\text{flow}})\|_2^2 \right] \quad [39]$$

an unbiased gradient estimator of the force matching loss.

**D. Reweighting of the flow samples to incorporate a pairwise repulsion.** Assuming that the CG potential implied by a trained flow model  $\mathcal{V}(\mathbf{r}, \boldsymbol{\eta}; \boldsymbol{\theta}_{\text{flow}})$  lacks a repulsion term  $U_{\text{repul}}$ , we aim for obtaining samples that follows the Boltzmann distribution according to a more physical CG potential  $\mathcal{V}(\mathbf{r}, \boldsymbol{\eta}; \boldsymbol{\theta}_{\text{flow}}) + U_{\text{repul}}$  by free-energy perturbation (74). For convenience, we let  $U_0 := \mathcal{V}(\mathbf{r}, \boldsymbol{\eta}; \boldsymbol{\theta}_{\text{flow}})$  and  $\Delta U := U_{\text{repul}}$  and omit the dependency on augmented variable  $\boldsymbol{\eta}$  for the derivation below.

The possibility for observing a certain CG conformation  $\mathbf{r}$ , i.e., the Boltzmann weight according to a potential  $U_0$ , is

$$p_0(\mathbf{r}) = \frac{1}{Z_0} e^{-\beta U_0(\mathbf{r})}, \quad Z_0 = \int_{\Gamma_0} e^{-\beta U_0(\mathbf{r}')} d\mathbf{r}'. \quad [40]$$

Similarly, we have the Boltzmann weight for  $U_0 + \Delta U$ :

$$p_1(\mathbf{r}) = \frac{1}{Z_1} e^{-\beta [U_0(\mathbf{r}) + \Delta U(\mathbf{r})]}, \quad Z_1 = \int_{\Gamma_1} e^{-\beta [U_0(\mathbf{r}') + \Delta U(\mathbf{r}')] } d\mathbf{r}'. \quad [41]$$

When the  $\Delta U$  is finite, the phase spaces  $\Gamma_0$  and  $\Gamma_1$  are identical, and we have:

$$Z_1 = \int_{\Gamma_0} e^{-\beta [U_0(\mathbf{r}') + \Delta U(\mathbf{r}')] } d\mathbf{r}' = Z_0 \int_{\Gamma_0} e^{-\beta \Delta U(\mathbf{r}')} d\mathbf{r}'. \quad [42]$$

(Note that even when the repulsion energy goes to infinity on a zero-measure set where two particles overlap  $\{\mathbf{r} \ni j, k \in \text{particles}, \text{ s.t. } \vec{r}_j = \vec{r}_k\}$ , e.g., for a  $1/d^p$  or LJ-like repulsion, the above equality still holds.) Therefore, we can evaluate  $p_1$  if we know  $p_0$  for any given conformation  $\mathbf{r}$ :

$$p_1(\mathbf{r}) = \frac{[p_0(\mathbf{r}) \cdot Z_0] e^{-\beta \Delta U(\mathbf{r})}}{Z_1} \quad [43]$$

$$= p_0(\mathbf{r}) \left[ e^{-\beta \Delta U(\mathbf{r})} \cdot \frac{Z_0}{Z_1} \right] \quad [44]$$

$$= p_0(\mathbf{r}) \cdot \underbrace{\int_{\Gamma_0} \frac{e^{-\beta \Delta U(\mathbf{r})}}{e^{-\beta \Delta U(\mathbf{r}')}} d\mathbf{r}'}_{\text{reweighting factor}} \quad [45]$$

The underlined expression is the reweighting factor that connects the original potential  $U_0$  and the perturbed potential  $U_0 + \Delta U$ . Given a set of coordinates  $\{\mathbf{r}_i\}$  sampled from the flow (i.e.,  $U_0$ ), we can approximate the reweighting factor by:

$$w_i = \int_{\Gamma_0} \frac{e^{-\beta \Delta U(\mathbf{r}_i)}}{e^{-\beta \Delta U(\mathbf{r}')}} d\mathbf{r}' \quad [46]$$

$$\approx \frac{e^{-\beta \Delta U(\mathbf{r}_i)}}{\sum_l e^{-\beta \Delta U(\mathbf{r}_l)}}. \quad [47]$$

This factor can be used for training the secondary CGnet model, including computing the marginal mean and standard deviations of the bond and angle dimensions (for prior energy parameters) as well as computing the force matching loss. As an example, the reweighted force matching loss (cf. Eq. 11 in maintext) over a set of flow-samples  $\{(\mathbf{r}_i, \tilde{\mathbf{f}}_i)\}_N$  becomes:

$$\mathcal{L}(\boldsymbol{\theta}_{\text{pot}}) \approx \sum_{i=1}^N \frac{w_i}{N} \left\| \tilde{\mathbf{f}}'_i + \nabla_{\mathbf{r}} V(\mathbf{r}; \boldsymbol{\theta}_{\text{pot}}) \right\|_2^2, \quad [48]$$

in which the weights  $w_i$  is evaluated via Eq. 47 over the whole set of flow samples and the new force corresponds to the modified potential:

$$\tilde{\mathbf{f}}'_i(\mathbf{r}_i, \boldsymbol{\eta}_i) = -\nabla_{\mathbf{r}} [U_0 + \Delta U](\mathbf{r}_i) = \tilde{\mathbf{f}}_i - \nabla_{\mathbf{r}} [\Delta U](\mathbf{r}_i) = \tilde{\mathbf{f}}_i + \mathbf{f}_{\text{repul}}(\mathbf{r}_i). \quad [49]$$

## 2. Additional details on the models

**A. Normalizing flow architecture.** The normalizing flow architecture is sketched in Fig. 4. After transforming euclidean coordinates (xyz) into internal coordinates (IC) (32), we apply an inverse CDF transform onto bonds and angles (Fig. 4 a), such that they are mapped into the unit interval. For the inverse CDF, we assume bonds and angles to follow a truncated Gaussian distribution where the parameters (truncation bounds, mean, variance) are estimated from the data. These whitened ICs are then transformed together with the latent variables  $\boldsymbol{\eta}$  into uniform and Gaussian densities, respectively, using the trainable flow (Fig. 4 b). The trainable flow consists of an alternating stack of coupling(67, 68) and shuffling blocks (Fig. 4 c,d,e). The coupling blocks transform one group of variables (e.g., torsions) conditioned on the context (ctx) given by several other variables (e.g., bonds, angles and latent) (Fig. 4 e). The transforms themselves require parameters (**params**), which are computed as the output of a trainable conditioner neural network (NN) with the context

**Table 1. Flow-specific hyper-parameters used in the experiments**

System	Hidden units for NN	No. of torsion blocks	No. of latent dimensions
Capped-Alanine	128, 1024, 128	2	2
Fast-Folders	128, 1024, 128	4	2

as input (Fig. 4 e). The transformed variables have different domains. While bonds and angles are supported on the unit interval, the torsions are supported on a circle, and the latent variables on a real vector space. To satisfy topological constraints (38, 54, 75), the following transforms are used: for the latent variables we use simple affine transforms (68) (Fig. 4 i). For bonds and angles we rely on either spline (69) or smooth (54) transforms (Fig. 4 g-h). Both methods can also be extended to transforms on the unit circle with the “wrapping method” (54, 75) and thus applicable for torsion variables. The conditioner neural network is a simple two layer dense net (Fig. 4 f). If torsions are part of the context, we satisfy the periodic boundary condition by a projection onto a  $\sin/\cos$  basis before feeding them into the network.

Although the transformation of a certain feature in each coupling layer can be conditioned upon all other features (i.e., they serve as input to the NN), we generally used the following restricted version in our experiments. It is based on an assumption of hierarchical dependency among the internal coordinates and helps to reduce computational overhead. Here we walk through the construction details of all layers in reverse order, i.e., from prior distribution to the actual IC distribution. Note that each feature channel can also be divided in halves to encourage mixing.

1. Prior distributions, including the following channels
  - (a) T (torsional), A (angular), B (bond-length channels): uniform distribution
  - (b) AUG (latent/augmentation channels): normal distribution
2. Torsion flow (T1, T2 are two halves of an equal split of all torsion channels), consisting of two or four torsion blocks, each defined as
  - (a) AUG  $\leftarrow$  coupling flow (affine)– (T1, T2)
  - (b) T1  $\leftarrow$  coupling flow (smooth)– (T2, AUG)
  - (c) T2  $\leftarrow$  coupling flow (smooth)– (T1, AUG)
3. Angle flow (A1, A2 are two halves of an equal split of all angle channels A), consisting of two angle blocks, each defined as
  - (a) A1  $\leftarrow$  coupling flow (smooth)– (A2, T)
  - (b) A2  $\leftarrow$  coupling flow (smooth)– (A1, T)
4. Bond flow, consisting of one bond block defined as
  - (a) B  $\leftarrow$  coupling flow (spline)– (A, T)
5. IC handling, including
  - (a) Inverse CDF transforms on B and A (to a truncated normal distribution)
  - (b) Inverse IC transformation

The hyper-parameters for the experiments are given in Table 1.

**B. CGnet architecture.** The CGnet architecture (20) is used as the “student” model that distills coarse graining knowledge from the flow samples. Essentially, all the internal coordinates (i.e., bond lengths, angles and dihedral angles) as well as the pairwise distances between nonbonded bead pairs are computed for input conformations. After a Z-score layer for whitening, they are fed into a multilayer perceptron (MLP) with hyperbolic tangent ( $\tanh$ ) activation function of a fixed width. The output energy is obtained as a weighted sum of the MLP output and its negative gradient with respect to the input coordinates gives forces. The force matching error can be computed between the neural network prediction and the mapped CG force from all-atom reference and forms the loss function for training.

For capped alanine, we mostly followed the architectural choices of the original publication (20). The only difference we introduced was adding skip connections between the output of each layer except for the input and output layers. We found that such changes reduced number of the epochs necessary for training convergence, and the accuracy of resulted models are comparable with the reported behavior in Ref. (20) when trained on the ground truth forces from all-atom simulations. The choice for prior energy terms was kept intact: harmonic potential terms were exerted on the bond and angle features, whose parameters were based on the ground-truth statistics. For a fair comparison, the same set of hyperparameters were used for both the conventional CGnet and the Flow-CGnet models.

For coarse graining of fast folding proteins, we found it necessary to introduce a few changes, such that the CGnet could correctly learn the free energy landscape from the flow models. These changes include relaxing the Lipschitz regularization strength, changing the activation function to Sigmoid Linear Unit (SiLU) as well as increasing the number of CGnet layers. For chignolin increasing the number of layers led to overfitting. Therefore, we stayed with 5 layers for this special case. Similar to Wang et al.’s experiments on CG chignolin, a repulsion term between the nonbonded bead pairs proved to be necessary for maintaining a reasonable exclusion volume and excluding unphysical crashes (20). We found the numerical stability and the accuracy of estimated free energy surface from simulation were sensitive to the choice of function form as well as parameters for the repulsion. The final choice of repulsion turned out to be a  $C^\infty$  piece-wise function:

$$u_{\text{repul}}(\vec{r}_i, \vec{r}_j) = \begin{cases} 1600k_B T \cdot (d_{ij} - \sigma_{ij})^2 & \text{if } j > i + 1 \text{ and } d_{ij} < \sigma_{ij} \\ 0 & \text{otherwise} \end{cases}, \quad [50]$$

where  $d_{ij} := |\vec{r}_i - \vec{r}_j|$  and the endpoint  $\sigma_{ij} = 0.36$  nm for glycine-involved pairs and 0.42 nm for all other pairs. The potential is computed for every non-neighboring pairs in the CG molecule and the results are summed to give the repulsive prior term. Note that the same repulsion function was also used for reweighting flow samples, which is based on Section 1D of this SI.

A list of concrete hyperparameter choices can be found in Table 2.

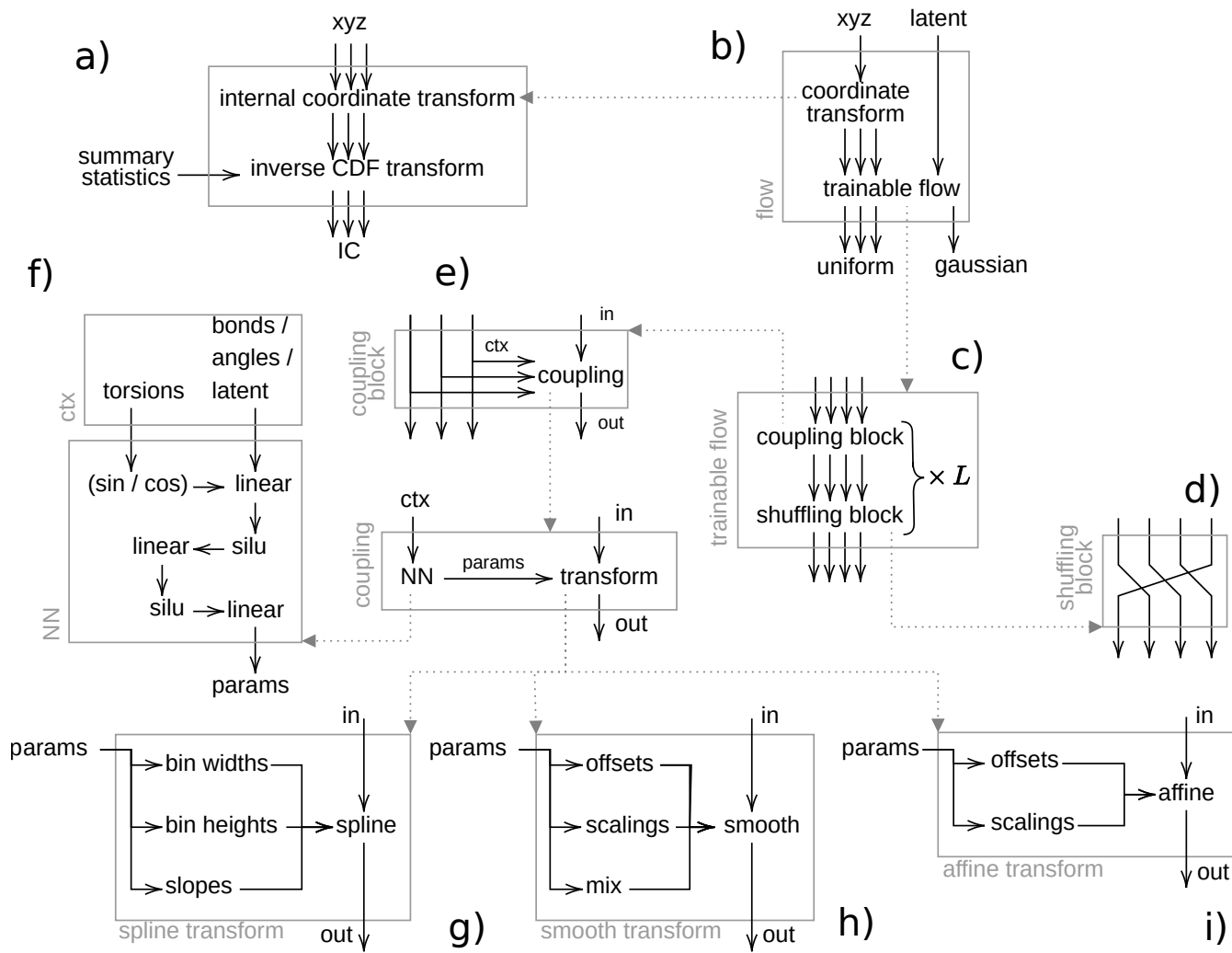


Fig. 4. Architecture of the normalizing flow.

Table 2. Hyperparameters of CGnets in the experiments

System	No. of fully connected layers	Neurons in each layer	Activation function	Lipschitz regularization strength	Prior terms
Capped-Alanine	5	160	tanh	4	Harmonic terms on bonds and angles
Fast-Folders	5 (chignolin) / 8 (others)	160	SiLU	10	Harmonic terms on bonds and angles + repulsion

### 3. Additional details on the experiments

**A. All-atom simulation for capped alanine.** The training set for capped alanine was generated in house with conventional all-atom MD simulations in OpenMM (76). The simulation system was set up according to Ref. (20). After equilibration at target temperature 300K for 10ns, the peptide coordinates and forces were recorded with a 2-ps interval. We performed four independent simulation runs starting from different initial structures. Each run is of length 500 ns, resulting in four times 250,000 sample points.

**B. Flow training, sample generation and post processing.** For capped alanine, the batch size for flow model training was set to 256. ADAM optimizer (77) was used and the learning rate was set to 0.001. We performed a four-fold cross validation by picking each trajectory in turn for validation, while using samples from the remaining three for training. In order to evaluate the scaling behavior of models with respect to the numbers of available training samples, models were obtained from training sets with different sizes, ranging from the maximum available 750,000 down to 10,000. The subsampling was done with random sampling. Training was performed for different number of epochs with respect to the training set sizes:

- 750,000 and 500,000: 30 epochs,
- 200,000: 75 epochs,
- others: 100 epochs.

For the fast folding proteins, the batch size was 128 and the maximum epoch number was uniformly 50.

The negative log likelihood of the flow on validation set is computed after each training epoch. Convergence in the validation loss was observed for all cases. The set of weights corresponding to the lowest validation loss was saved as checkpoint and 1,048,576 samples were generated with the best model and forces are calculated accordingly.

For capped alanine, we chose to discard samples whose corresponding forces exceed  $\sqrt{1.5 \times 10^5 k_B T / \text{nm}}$  in magnitude, which is defined as  $\sqrt{\frac{1}{N} \sum_i \|\mathbf{f}\|_2^2}$ . For fast folding proteins, we filtered the samples with an upper limit for force magnitude of  $\sqrt{8 \times 10^4 k_B T / \text{nm}}$ , and then computed the weights for the remaining samples according to the repulsion term introduced in Section S2B and expression in S1D. The weights were used to compute the statistics for defining the harmonic prior terms for Flow-CGnets and the weighted force-matching error for training and validation.

Despite the importance of the filtering and reweighting on the quality of Flow-CGnet outcome, these post-processing measures only marginally affect the distribution on the dihedral and TICA landscapes as well as the RMSD distributions. Therefore, the original flow samples were used for distribution plotting and analysis without reweighting.

**C. Flow-CGnet training.** The CGnet training for capped alanine used ADAM optimizer as well. The batch size was 128 and initial learning rate was 0.003. An exponential decay was applied on the learning rate every 5 epochs, such that the target learning rate  $10^{-5}$  was reached in 50 epochs. The incoming flow samples were randomly shuffled and then divided according 80%–20% ratio for training and validation sets. Model checkpoints were saved every two epochs at the epochal end, from which the one with minimum force matching loss on the validation set was used for later simulation. The training of Flow-CGnet for fast folders followed essentially the same setup, expect that the learning rate decayed every 15 epochs over 75 training epochs in total, and the loss calculation was based on repulsion-reweighting.

**D. CGnet simulations.** The friction constant for CG Langevin dynamics is set to  $1 \text{ ps}^{-1}$ . For capped alanine, we performed 2-ns parallel tempering (PT) simulations for both Flow-CGnet and conventional CGnet models. For fast folding proteins, we performed both 50-ns PT and 50-ns normal Langevin simulations. The exchange-proposing interval for PT simulations is 2 ps for capped alanine and 5 ps for fast folding proteins. In simulations, 100 independent trajectories were obtained in parallel for each molecule, so as for accumulating sufficient samples with reduced computational overhead for each time step.

**E. tICA coordinates.** For a low-dimensional comparison between coarse-grained and atomistic models, we performed time-lagged independent component analysis (tICA) (50–52) using deeptime (78). As features, we computed all pairwise distances between  $C_\alpha$  atoms as well as all dihedral angles between every four consecutive  $C_\alpha$  atoms in a protein chain. Time-lagged feature covariances were computed using a lagtime of 20 ns (100 frames) for each set of trajectories from (5). This choice of lag time enables recognizing all mean transition path times, which range from 40 to 700 ns for the considered trajectories. The data was projected on the two slowest modes (corresponding to the highest eigenvalues) for plotting and further analysis.